



Multi-scale topology optimization for stiffness and de-homogenization using implicit geometry modeling

Groen, J. P.; Thomsen, C. R.; Sigmund, O.

Published in:
Structural and Multidisciplinary Optimization

Link to article, DOI:
[10.1007/s00158-021-02874-7](https://doi.org/10.1007/s00158-021-02874-7)

Publication date:
2021

Document Version
Peer reviewed version

[Link back to DTU Orbit](#)

Citation (APA):
Groen, J. P., Thomsen, C. R., & Sigmund, O. (2021). Multi-scale topology optimization for stiffness and de-homogenization using implicit geometry modeling. *Structural and Multidisciplinary Optimization*, 63, 2919–2934 .
<https://doi.org/10.1007/s00158-021-02874-7>

General rights

Copyright and moral rights for the publications made accessible in the public portal are retained by the authors and/or other copyright owners and it is a condition of accessing publications that users recognise and abide by the legal requirements associated with these rights.

- Users may download and print one copy of any publication from the public portal for the purpose of private study or research.
- You may not further distribute the material or use it for any profit-making activity or commercial gain
- You may freely distribute the URL identifying the publication in the public portal

If you believe that this document breaches copyright please contact us providing details, and we will remove access to the work immediately and investigate your claim.

Multi-scale topology optimization for stiffness and de-homogenization using implicit geometry modeling

J.P. Groen · C.R. Thomsen · O. Sigmund

Received: date / Accepted: date

Abstract In this article we demonstrate the state-of-the-art of multi-scale topology optimization for 3D structural design. Many structures designed for additive manufacturing consist of a solid shell surrounding repeated microstructures, so-called infill material. We demonstrate the performance of different types of infill microstructures, such as isotropic truss- or plate lattice structures and show that the best results can be obtained using spatially varying and oriented orthotropic microstructures. Furthermore, we demonstrate how implicit geometry modeling using nTop platform can help to interpret these multi-scale designs as single-scale manufacturable designs (de-homogenization). More importantly, we demonstrate the small difference in performance between these multi-scale and single-scale designs through extensive numerical testing. The presented method is at least 3 orders of magnitude more efficient compared to standard density-based topology optimization, allowing for high-resolution 3D structures to be obtained on a standard workstation PC.

Keywords Topology Optimization · De-homogenization · Implicit geometry · Microstructures

1 Introduction

Topology optimization is a well-established design method with many applications both in academia and in industry. Hence, nearly all major modern

computer-aided design (CAD) software, contains methods for density-based optimization possibilities and/or shape optimization, *e.g.* Ansys Inc (2020); Autodesk Inc (2020); COMSOL Inc (2019); Dassault Systèmes (2020); nTopology Inc (2020). The increase in applicability of topology optimization can partially be attributed to the rapid increase in design freedom offered by novel additive manufacturing (AM) techniques, and partly by the availability of computational resources to allow for large-scale 3D design. Nevertheless, large-scale topology optimization still comes at a high computational cost. Recently, Aage et al. (2017) extended the state-of-the-art for compliance minimization problems by optimizing a full-scale airplane wing with more than 1 billion design variables, the largest element was at most 8mm on a wing with a half wingspan of 27m. However, to do so, 8000 cores were employed on a high performance computer (HPC) system for up to 5 days.

A possibility to reduce the cost is to perform multi-scale topology optimization, subsequently followed by a de-homogenization step in which the multi-scale design is approximated on a single-scale (Pantz and Trabelsi, 2008; Groen and Sigmund, 2018; Geoffroy-Donders et al., 2020b). Recent results for compliance minimization subject to a single loading case by Groen and Sigmund (2018) and Groen et al. (2019, 2020) indicate a similar performance for the de-homogenized and multi-scale designs, and a reduction in computational cost compared to standard density-based topology optimization of 2 orders of magnitude in 2D and at least 3 orders of magnitude in 3D.

It is well-known that the theoretically optimal shape for a compliance minimization problem contains periodic details on several length-scales (Kohn and Strang, 1986; Allaire and Aubry, 1999). Furthermore, it is known that the class of so-called rank-

J.P. Groen · O. Sigmund
Department of Mechanical Engineering, Technical University of Denmark, 2800 Kgs, Lyngby, Denmark
E-mail: jeroenisgroen@gmail.com

C.R. Thomsen
nTopology inc. 101 Avenue of the Americas 12th floor, New York, NY 10013, USA

N laminates can reach the bounds on maximum strain energy for microstructures (Lurie and Cherkayev, 1984; Milton, 1986; Norris, 1985; Francfort and Murat, 1986). Using the theory of homogenization (Bensoussan et al., 1978) we can calculate the macroscopic properties of these microstructures analytically and use them to perform topology optimization (Allaire, 2002; Bendsøe and Sigmund, 2004). Nevertheless, the interest in homogenization-based topology optimization using rank- N laminates has decreased over the past two decades due to the fact that multi-scale microstructures cannot be directly manufactured. Only recently, with the increase in research in de-homogenization methods Geoffroy-Donders (2018); Groen (2019) and single-scale interpretations of optimal microstructures (Träff et al., 2019; Wang and Sigmund, 2019), there has been a renewed interest in rank- N microstructures.

The first paper on topology optimization by Bendsøe and Kikuchi (1988) actually considered multi-scale topology optimization using single-scale microstructures resulting in a performance very similar to optimal rank-2 microstructures. For multiple loading cases a more general multi-scale topology optimization was introduced by Rodrigues et al. (2002). In this approach each macroscopic element represents a uniform periodic single-scale microstructure that is optimized using inverse homogenization (Sigmund, 1994) for the stresses/strains acting on that specific element. Although this multi-scale method works well it has two major downsides: 1) compared to rank- N laminates a very large number of design variables needs to be considered and 2) the microstructures in adjacent elements are not connected and hence the multi-scale design cannot be manufactured.

To reduce the computational cost one can restrict the amount of allowable microstructures (Sivapuram et al., 2016); however, this results in a reduced performance and does not say anything about connectivity. Although Zhou and Li (2008) and Du et al. (2018) have enforced connectivity between microstructures, the actual load transfer is never verified through full-scale analysis. Only recently, Garner et al. (2019) did a microstructure design also optimized for efficient load transfer between adjacent microstructures. To avoid the large number of constraints to ensure load-transfer between adjacent microstructures one can either use a uniform microstructure in the entire domain (Huang et al., 2013) or distinguish between void and this uniform microstructure Liu et al. (2008); however, both approaches are very far from optimal. The use of graded microstructures allows for slightly more freedom and better connectivity (Cramer et al., 2015; Wang et al., 2017).

In above-mentioned de-homogenization approaches an implicit geometry description is used to obtain well-connected microstructures that represent the homogenization-based design. In a similar fashion, Jiang et al. (2020) have used a conformal map to generate connected microstructures; however, since the microstructure orientation is not included in the optimization this mapping is only for visual post-processing means. In a different approach Liu et al. (2017); Xue et al. (2020) do not create the implicit geometry description in a post-processing step, but directly optimize the geometry description using global perturbation functions; however, it should be noted that this approach can easily get stuck in a local minimum due to the non-local design descriptions.

Interestingly, few of the above-mentioned approaches consider an actual full-scale analysis to identify whether a single-scale approximation of the multi-scale design is useful in engineering practice. To the authors knowledge only the works of Zhang and Sun (2006); Pantz and Trabelsi (2008); Zuo et al. (2013); Liu et al. (2017); Groen and Sigmund (2018); Garner et al. (2019); Groen et al. (2019); Kumar and Suresh (2019); Wu et al. (2019); Groen et al. (2020); Xue et al. (2020); Jiang et al. (2020) actually do such an important full-scale verification. This can be seen as a missed opportunity, especially since many works claim to do topology optimization to allow for additive manufacturing (AM). In the context of AM many structures consist of a solid outer shell reinforced by periodic infill patterns. Although many works on multi-scale topology optimization consider simultaneous design of outer shell and infill microstructures, *e.g.* (Vermaak et al., 2014; Clausen et al., 2015; Wang and Kang, 2018; Fu et al., 2019; Jiang et al., 2019; Luo et al., 2019; Geoffroy-Donders et al., 2020a) only the works of Clausen et al. (2016); Wu et al. (2017) and Groen et al. (2019) consider actual physical or numerical testing of the performance of a coated structure reinforced by periodic infill. Finally, it should be mentioned that besides multi-scale topology optimization, Alexandersen and Lazarov (2015) were able to accurately and efficiently model a large amount of repeated microstructures using a multi-scale finite element method.

In this paper we consider multi-scale topology optimization of 3D structures to minimize compliance subject to a single loading case and under the assumption of linear elasticity. The main focus is to achieve well-connected designs that can be verified. Although the designs have a minimum feature size, we have not included any other constraints related to *e.g.* additive manufacturing. A reader interested in the different methods to manufacture topology optimized designs and the cur-

rent challenges is referred to the works by Brackett et al. (2011), and Liu et al. (2018).

Our main contribution is that we improve and discuss the entire workflow, *i.e.* from micro-structure parameterization and homogenization-based topology optimization to full-scale validation of the de-homogenized designs. Through numerical experiments we quantify the effect of different types of microstructures on the performance of a multi-scale design, both in the context of coated designs as well as non-coated designs. Subsequently, we show how these multi-scale designs can be interpreted (de-homogenized) on a single length-scale to produce well-connected structures. Most importantly, we demonstrate the small difference in performance between multi-scale analysis and a full-scale analysis of de-homogenized design to show that multi-scale topology optimization and subsequent de-homogenization is an efficient and effective method to generate high-resolution and high-quality designs. An overview of these steps is given in Figure 1. All of the results in this work are obtained on a modern workstation PC, eliminating the need for HPC facilities. Finally, it should be mentioned that the research on efficient de-homogenization is done using nTop Platform (nTopology Inc, 2020) to demonstrate how industry and academia can support each other to advance the field of multi-scale topology optimization.

This article is organized as follows: different microstructures to perform homogenization-based topology optimization and a short summary of the theory to perform homogenization-based topology optimization are given in Section 2. Numerical experiments comparing the performance difference between the microstructures are discussed in Section 3. A brief overview of de-homogenization and the corresponding experiments on the performance between single-scale and multi-scale designs are discussed in 4. Finally, the most important conclusions of each of the different studies will be summarized in Section 5.

2 Homogenization-based topology optimization

Optimal design for compliance minimization requires rank- N laminates, see *e.g.* (Allaire, 2002). For a 3D design domain and a single loading case, orthogonal rank-3 laminates are sufficient to parameterize the space of optimal materials (Gibiansky and Cherkaev, 1987). For an optimization example with multiple independent loading cases at most 6 lamination directions are required, *e.g.* an isotropic microstructure requires a rank-6 laminate. Although rank- N laminates are optimal microstructures, they are built up on several length-scales.

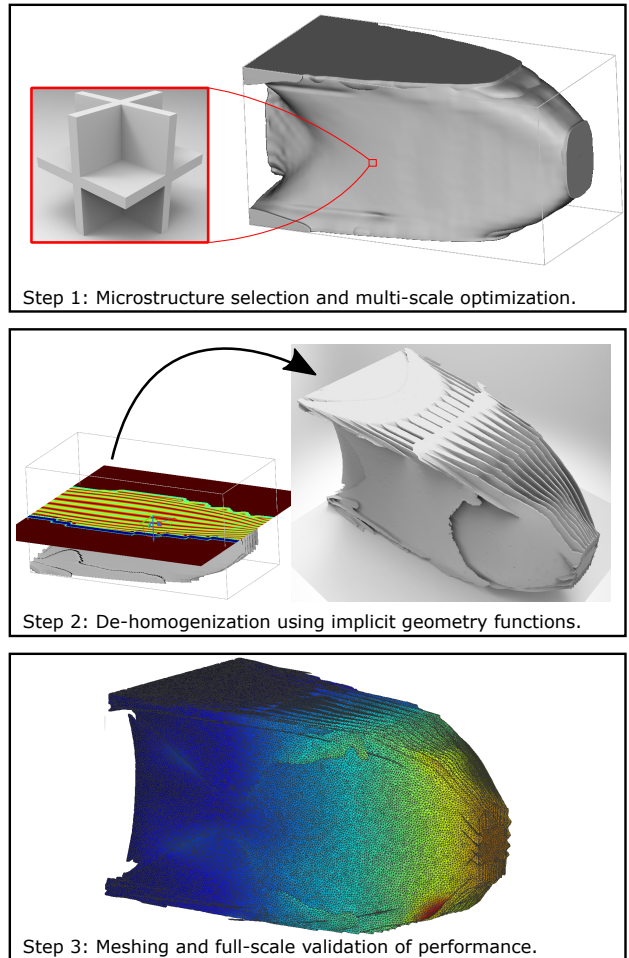


Fig. 1: Overview of the multi-scale topology optimization and de-homogenization procedure. Both de-homogenization and full-scale validation are performed with nTop platform (nTopology Inc, 2020).

Hence, for manufacturability a single-scale interpretation has to be found. Below we will discuss several single-scale microstructure parameterizations and how these microstructures can be used for multi-scale topology optimization. However, it should be remarked that this single-scale interpretation inevitably will result in sub-optimal designs (Allaire and Aubry, 1999).

2.1 Interpolation of materials and microstructures

The first microstructure that is considered is the single-scale approximation of an orthogonal rank-3 laminate (SSR3), which is shown in Figure 2(a). As discussed in (Groen et al., 2020) there exists a relation between the hierarchical relative layer widths μ_i , used to describe a rank-3 laminate, and the widths w_i of the single scale approximation of a rank-3 microstructure.

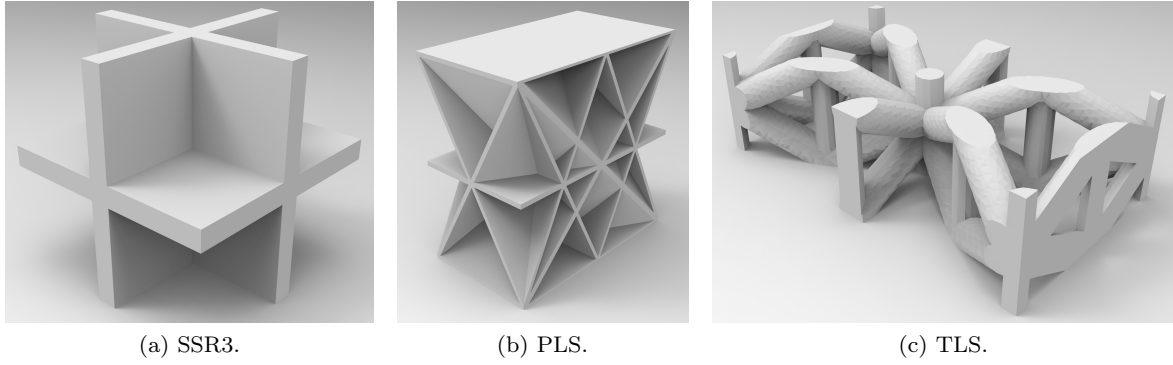


Fig. 2: Different microstructures considered in this study. All visualized for a single period and a volume fraction of $\rho = 0.25$.

The orthotropic elasticity tensors \mathbf{E}^{SSR3} can be analyzed for different lamination widths w_1 , w_2 and w_3 resulting in a database of $11 \times 11 \times 11$ combinations for $w_i \in [0.025, 0.5]$, for $i = 1, 2, 3$. For the parameterization and numerical homogenization we have used nTop platform, with meshes consisting of approximately 0.5-1 million tetrahedral elements using quadratic shape functions. As a base material we use an isotropic material with $E = 1$ and $\nu = 0.3$. The corresponding three unique indices of \mathbf{E}^{SSR3} for $w_1 = w_2 = w_3$ are shown in Figure 3 as well as the reference values for the multi-scale rank-3 microstructures.

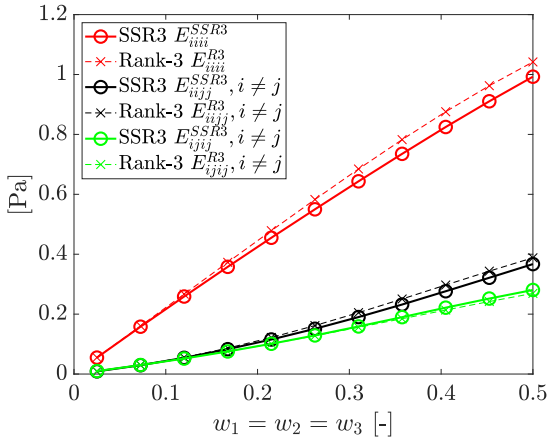


Fig. 3: Unique indices of the elasticity tensor of a rank-3 laminate and single-scale (SSR3) interpretation for $w_1 = w_2 = w_3$.

As expected the single-scale approximation has slightly more shear stiffness, but lower stiffness in each of the direction of the material frame of reference than its multi-scale counterpart. To obtain the elasticity ten-

sor \mathbf{E} in the global frame of reference \mathbf{x} we use rotation tensor \mathbf{R} that describes the transformation of a first order tensor from local frame of reference \mathbf{y} to global frame of reference \mathbf{x} based on three Euler angles $(\theta_1, \theta_2, \theta_3)$,

$$E_{ijkl} = R_{im}R_{jn}R_{ko}R_{lp}E_{mnop}^{SSR3}. \quad (1)$$

Finally, to interpolate for values of w_i in between the calculated elasticity tensors we apply a piece-wise linear interpolation.

Although sub-optimal many AM processes use a repeated isotropic infill material, either using open truss lattice structures (TLS) or closed plate lattice structures (PLS). It has been long known that multi-scale PLS provide optimal stiffness to weight ratio, *i.e.* they satisfy the Hashin-Shtrikman bounds for isotropic microstructures (Hashin and Shtrikman, 1963), and in the limit are three times stiffer than TLS (Christensen, 1986; Wang et al., 2019). For this study we use the near-optimal single-scale approximations of the optimal PLS that have been proposed by Wang and Sigmund (2019). A 6-fold isotropic PLS can be seen in Figure 2(b) and its corresponding dual the isotropic TLS can be seen in Figure 2(c). More details on how these microstructures are built up can be found in Wang and Sigmund (2019).

For both microstructures we have performed numerical homogenization for various values of ρ . For the TLS we have used approximately 100k-200k tetrahedral elements and for the PLS 200k-400k both using quadratic shape functions. The corresponding first two Lamé parameters λ and G are shown in Figures 4(a) and (b) for the different values of ρ . Since the microstructures are (nearly) isotropic we have used the averaged values of

\tilde{E}_{1111} and \tilde{E}_{1122} , which are obtained using,

$$\begin{aligned}\tilde{E}_{1111} &= \frac{E_{1111} + E_{2222} + E_{3333}}{3}, \\ \tilde{E}_{1122} &= \frac{E_{1122} + E_{1133} + E_{2233}}{3}.\end{aligned}\quad (2)$$

Besides the microstructure responses, we have also plotted the Hashin-Shtrikman bounds for isotropic microstructures (Hashin and Shtrikman, 1963) and the Solid Isotropic Microstructure with Penalization (SIMP) method for a penalty value of 3 (Bendsøe and Sigmund, 2004). It can be seen that the PLS perform close to the Hashin-Shtrikman bounds, even for moderate densities. Furthermore, it can be seen that the difference in stiffness between the PLS and TLS becomes smaller when larger volume fractions are considered. However, it should be noted that the PLS is always performing better.

Finally, we verify the isotropy deviation of each microstructure. To do this we use the universal isotropy index M^U as proposed by Ranganathan and Ostoj-Starzewski (2008). Details on the calculation of this measure are given in Appendix A. A microstructure is perfectly isotropic for $M^U = 0$, hence Figure 4(c) shows that the PLS are nearly perfectly isotropic. The TLS have a slight deviation from isotropy for higher volume fractions; nevertheless, this difference can be considered small. On the contrary, the SSR3 microstructure using $w_1 = w_2 = w_3$ has an isotropy index $M^U = 0.8722$ for $\rho = 0.1$ and $M^U = 0.6089$ for $\rho = 0.3$ which demonstrates the significant deviation away from isotropy. Similar to the SSR3 microstructures, we use a piecewise linear interpolation for the isotropic elasticity tensors of the TLS and PLS.

2.2 Topology optimization formulation

The theory to perform multi-scale topology optimization to minimize compliance \mathcal{J} , in the context of linear elasticity is discussed in (Groen, 2019) and (Groen et al., 2020) and will therefore be kept brief in this work. We parameterize a design domain Ω using $n_1 \times n_2 \times n_3$ tri-linear finite element, where each element can represent a different homogenized microstructure. We use design vector \mathbf{x} to describe the spatially varying design, *e.g* the density distribution $\boldsymbol{\rho}$ if the SIMP method or the isotropic PLS and TLS are used to parameterize the

design. The topology optimization problem is solved in nested form and its general form can be written as,

$$\begin{aligned}\min_{\mathbf{x}} : \mathcal{F}(\mathbf{x}, \mathbf{U}) &= \frac{\mathcal{J}(\mathbf{x}, \mathbf{U})}{\mathcal{J}^0} + \gamma_\theta \mathcal{F}_\theta(\mathbf{x}), \\ \text{s.t.} : \mathbf{K}(\mathbf{x})\mathbf{U} &= \mathbf{F}, \\ : \mathbf{v}^T \boldsymbol{\rho}(\mathbf{x}) - V_f^{max} V &\leq 0, \\ : \mathbf{x}_{low} \leq \mathbf{x} \leq \mathbf{x}_{upp},\end{aligned}\quad (3)$$

here the compliance \mathcal{J} is normalized with the performance \mathcal{J}^0 of the starting guess. If design vector \mathbf{x} also contains information about the orientation of the SSR3 we can regularize the orientation using an augmented objective \mathcal{F}_θ . More information about this regularization objective and the corresponding scaling factor γ_θ can be found in (Groen et al., 2020). Furthermore, vector \mathbf{v} contains the element volumes and V_f^{max} is the maximum allowed fraction of the material in Ω , with V the volume of Ω . \mathbf{K} is the stiffness matrix and vector \mathbf{F} describes the loads acting on the domain. We solve for the displacement vector \mathbf{U} using a conjugate gradient method in combination with a geometrical multi-grid pre-conditioner (Amir et al., 2013). \mathbf{x}_{low} and \mathbf{x}_{upp} describe the lower and upper bounds on the design vector \mathbf{x} respectively. For the design update the MATLAB implementation of the Method of Moving Asymptotes (MMA) introduced by Svanberg (1987) is used. It should be noted that artificially stiff checkerboard patterns are avoided using a density filter (Bourdin, 2001; Bruns and Tortorelli, 2001) with a filter radius of $R = 1.5 h$ with h the length of a finite element.

3 Numerical performance of multi-scale designs

In this paper we will study a clamped beam subject to a corner load as shown in Figure 5(a) and the Michell cantilever shown in Figure 5(b). The homogenization-based topology optimization step is performed on a modern PC using a single core MATLAB code. The PC uses Ubuntu 16.04.6 and contains an Intel Xeon Platinum 8160 processor with 64 GB RAM memory.

First, we consider the clamped beam subject to a corner load, where the downwards force is applied at an area of $L/10 \times L/10$. For this structure we consider two cases, 1) a coated design, where the outer part of the design domain is solid with a coating thickness of $L/20$, with $V_f^{max} = 0.25$ for the non-coated part, and 2) a non-coated design using $V_f^{max} = 0.33$. Hence, the coated design consists of more material with a total volume fraction $V_f^{max} = 0.428$ for the total design domain. We compare the difference in homogenization-based compliance \mathcal{J}^c for five different types of microstruc-

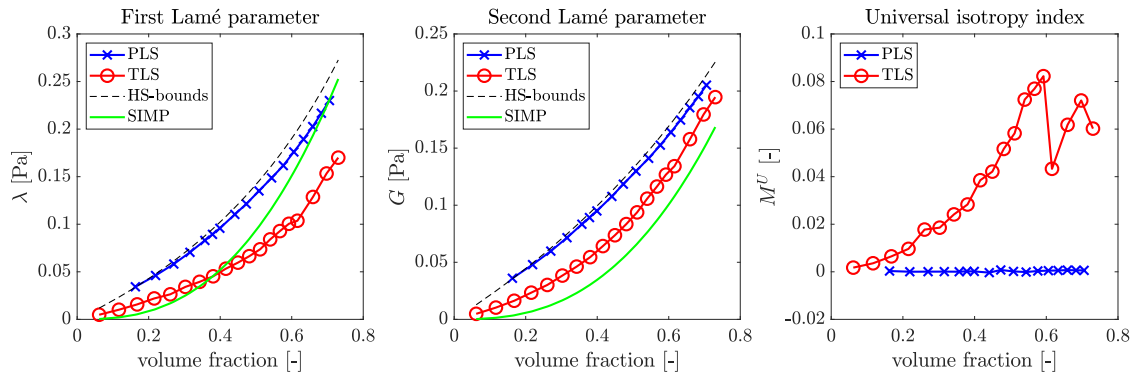


Fig. 4: Lamé parameters and the universal isotropy index M^u for the isotropic truss lattice structure (TLS) and plate lattice structure (PLS).

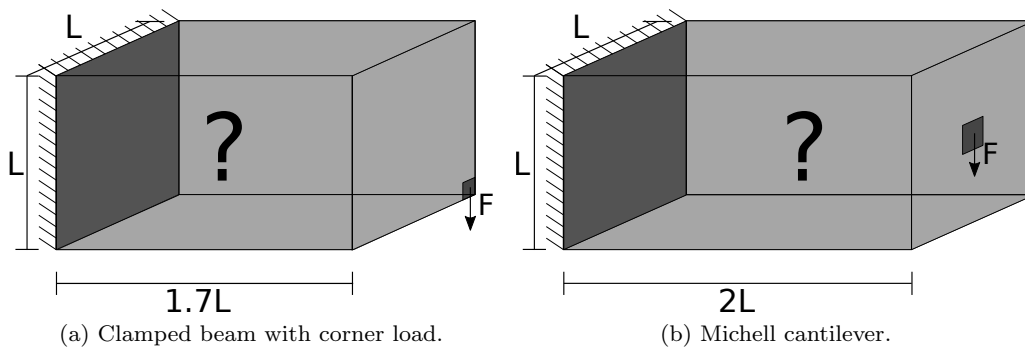


Fig. 5: Dimensions and boundary conditions for the numerical examples used in this work.

tures: an optimal orthogonal rank-3 laminate, the corresponding single-scale approximation SSR3, the TLS, the PLS, and a uniform rank-6 microstructure. For each of the microstructures we consider different variations, *e.g.* allowing the orientation to vary or to keep the density ρ uniform throughout the design domain. These different variations allow us to compare many different types of optimization formulations and analyze their differences. Furthermore, we show the performance of a design obtained using the well-known SIMP method with a continuation on the penalty parameter. The numerical examples have all been performed on a coarse mesh \mathcal{T}^c consisting of $40 \times 68 \times 40$ elements, corresponding compliance values \mathcal{J}_1^c and \mathcal{J}_2^c for case 1 (coated) and case 2 (non-coated), respectively, can be seen in Table 1.

A "varying" orientation means that each microstructure is allowed to have a spatially varying orientation, while a "fixed" microstructure orientation means that the microstructure frame of reference is identical to the global frame of reference. The same is the case with a varying density ρ or a uniform density in each microstructure. For the case of a SSR3 microstructure a fixed density does not necessarily mean that the layer

widths are not allowed to change. Finally, a design with a uniform rank-6 microstructure is modeled. This is to show that even this microstructure that can reach the theoretical bounds on stiffness is sub-optimal compared to a spatially varying design.

First of all, and in agreement with Figure 3, it can be seen in Table 1 that the difference between the rank-3 microstructure and the SSR3 is small. Second, and as expected, the structure with a coating will give much better compliance values, since the coating gives torsional rigidity to the design. Although the current loading case is very simple, it can be seen that there is a large difference in the performance for different restrictions to the SSR3. Especially, having a fixed microstructure density throughout the design domain reduces the performance. Actually, it can be seen that having a microstructure with any type of restriction will result in a worse performance than a single-scale design obtained with the SIMP method. Furthermore, it is clear that the PLS are much stiffer than the TLS. Hence, when only stiffness is considered close-walled microstructures are much more optimal. However, open-walled microstructures may be optimal for other aspects, such as stability (Andersen et al., 2020). It can be observed that

Table 1: Compliance values for coated \mathcal{J}_1^c and non-coated \mathcal{J}_2^c multi-scale designs of the cantilever s.t. a corner load (Figure 5(a)). Different microstructures are used as well as different variations on the design freedom to demonstrate the effect on the performance.

Microstructure	Orientation	Density	Other restrictions	\mathcal{J}_1^c	\mathcal{J}_2^c
Rank-3	varying	varying	$\mu_i \in [0.025, 0.5]$	82.228	93.604
SSR3	varying	varying	$w_i \in [0.025, 0.5]$	82.932	96.420
SSR3	fixed	varying	$w_i \in [0.025, 0.5]$	86.576	102.908
SSR3	varying	fixed	$w_i \in [0.025, 0.5]$	97.472	183.256
SSR3	fixed	fixed	$w_i \in [0.025, 0.5]$	102.240	211.256
SSR3	varying	varying	$w_1 = w_2 = w_3 \in [0.025, 0.5]$	84.908	100.124
SSR3	fixed	varying	$w_1 = w_2 = w_3 \in [0.025, 0.5]$	88.828	107.044
SSR3	varying	fixed	$w_1 = w_2 = w_3 \in [0.025, 0.5]$	101.732	227.088
SSR3	fixed	fixed	$w_1 = w_2 = w_3 \in [0.025, 0.5]$	113.660	301.092
TLS	fixed	varying	$\rho \in [0.1, 0.7]$	101.300	339.972
TLS	fixed	fixed	$\rho \in [0.1, 0.7]$	126.240	526.196
PLS	fixed	varying	$\rho \in [0.1, 0.7]$	93.912	225.588
PLS	fixed	fixed	$\rho \in [0.1, 0.7]$	110.512	300.960
Rank-6	uniform	uniform	$\mu_i \in [0.0, 1.0]$	97.768	215.612
SIMP	fixed	varying	$\rho \in [0.0, 1.0]$	79.418	82.808

the uniform rank-6 microstructure has a similar performance as the graded PLS microstructure. It is expected that for a more complex loading case than the current one, the graded PLS will outperform the single-scale rank-6. Hence, in general it is advised to avoid using a single uniform microstructure in the domain. Finally, as will be elaborated on in the next Section, it is possible to interpret all designs on a single-scale. The large difference in performance even for a simple load-case as the current one shows the importance of using the correct microstructure. Hence, it always pays off to investigate which type of microstructure is best for a specific set of loads and boundary conditions.

The second example that we discuss is the cantilever shown in Figure 5(b). This example is optimized on a mesh of $48 \times 96 \times 48$ elements using $V_f^{max} = 0.10$. First, we show the possible performance using optimal rank-3 microstructures with no bounds on the layer widths (see *e.g.* Groen et al. (2020)). Afterwards, we show the effect of setting bounds on the layer widths for both the rank-3 microstructure and the SSR3. Furthermore, we show the performance when uniform TLS or PLS microstructures are used with $\rho = 0.10$ and show the performance using a uniform rank-6 microstructure and the SIMP method. Corresponding compliance values \mathcal{J}^c , number of iterations n_{iter} and run time T^{opt} can be seen in Table 2.

It is interesting to see that the compliance is around 30–40% higher compared to the optimal solution when the lamination widths are restricted. Hence, any restriction of a microstructure parameterization will significantly move away from optimality and the microstructure parameterization thus has to be carefully selected for each optimization example. Especially, since in many

cases a single-scale design using the SIMP method will produce a better performing structure, see *e.g.* Figure 9(a) for the non-coated case. Finally, it should be mentioned that the rank-6 microstructure for this load-case consists of thick plates in the x_1x_2 -plane, and therefore is more optimal than the uniform PLS. However, it should be noted that the more complex the loading situation, (*e.g.* multiple load cases) the closer the rank-6 microstructure will become to isotropy (Wang et al., 2019).

4 Multi-scale versus single-scale performance

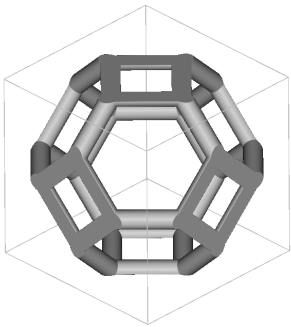
We perform multi-scale topology optimization to either get an analytical bound on the attainable compliance or to get a well-performing design consisting of complex microstructures in a short time. For the latter, it is important to study 1) how we efficiently can get a manufacturable design out of the multi-scale design (de-homogenization) and 2) how well the performance of this single-scale design matches the multi-scale performance. To do so, we will discuss first how an implicit geometry description can help to de-homogenize a multi-scale model. Afterwards, we will demonstrate the difference between a multi-scale and single-scale model for two examples.

4.1 De-homogenization using an implicit geometry description

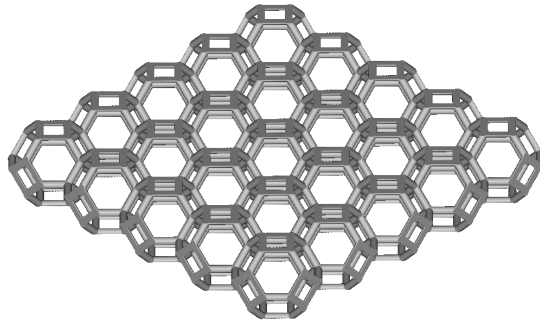
Using an implicit geometry representation, the boundary of a geometry is defined by the equation $\psi(\mathbf{x}) = 0$, where ψ is a scalar valued function. This can be related

Table 2: Mesh resolution, number of degrees of freedom n_{dof} , compliance values \mathcal{J}^c , number of design iterations n_{iter} and run time T^{opt} for the multi-scale designs of the Michell cantilever (Figure 5(b)) optimized for different microstructures.

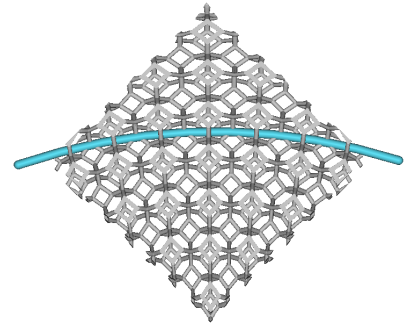
\mathcal{T}^c	$n_{dof}(\times 10^5)$	Microstructure	Restrictions	\mathcal{J}^c	n_{iter}	T^{opt}
$48 \times 96 \times 48$	6.99	Rank-3	$\mu_i \in [0, 1]$	226.68	400	09:45:35
$48 \times 96 \times 48$	6.99	Rank-3	$\mu_i \in [0.025, 0.5]$	306.72	358	09:16:38
$48 \times 96 \times 48$	6.99	SSR3	$w_i \in [0.025, 0.5]$	311.85	333	08:32:14
$48 \times 96 \times 48$	6.99	Rank-6 (uniform)	$\mu_i \in [0, 1]$	443.39	50	00:47:27
$48 \times 96 \times 48$	6.99	PLS	$\rho = 0.10$	753.69	1	00:01:08
$48 \times 96 \times 48$	6.99	TLS	$\rho = 0.10$	1824.44	1	00:00:55
$48 \times 96 \times 48$	6.99	SIMP	$\rho \in [0, 1]$	265.52	450	02:41:20



(a) Microstructure unit-cell.



(b) Uniform sequence.



(c) Spatially varying sequence.

Fig. 6: Implicit microstructure representation and different methods to repeat it in space.

to the density distribution ρ in topology optimization as,

$$\begin{aligned} \rho(\mathbf{x}) &= 1 & \text{if } \psi(\mathbf{x}) > 0, \\ \rho(\mathbf{x}) &= 0 & \text{if } \psi(\mathbf{x}) < 0. \end{aligned} \quad (4)$$

A signed distance function is a commonly used example of ψ , which satisfies the condition that $\|\nabla\psi\| = 1$. Using nTop platform (nTopology Inc, 2020) structures are designed using implicit geometry description rather than Non-uniform rational basis spline (NURBS) used in traditional CAD software. Compared to explicit NURBS-based geometry representations, an implicit geometry description possesses a number of advantages that are specifically beneficial to the design of infill structures. This includes robust Boolean operations such as unions, subtractions and intersection, and more importantly, efficient spatial geometry repetition. To demonstrate the latter, consider the microstructure with dimensions $\{10 \text{ mm}, 10 \text{ mm}, 10 \text{ mm}\}$ shown in its local frame of reference \mathbf{y} in Figure 6(a). The implicit geometry description in the local frame of reference $\psi(\mathbf{y})$ can be used to tessellate this microstructure in space in the global frame of reference \mathbf{x} using,

$$\psi(\text{mod}\{\mathbf{x}, 10 \text{ mm}\}), \quad (5)$$

were mod is the modulo operator. The corresponding sequence of microstructures intersected with a block of dimensions $\{50 \text{ mm}, 50 \text{ mm}, 10 \text{ mm}\}$ can be observed in Figure 6(b). Besides a uniform microstructure tessellation it is also possible to create a spatially varying map, based on mapping function $\phi = \{\phi_1, \phi_2, \phi_3\}$,

$$\psi(\text{mod}\{\phi(\mathbf{x}), 10 \text{ mm}\}). \quad (6)$$

Here ϕ can be based on three orthogonal vector fields $\{\mathbf{n}^1, \mathbf{n}^2, \mathbf{n}^3\}$. The theory to obtain ϕ from these vector fields is discussed in Appendix B (Groen et al., 2020). In Figure 6(c) we show a spatially varying sequence of microstructures where \mathbf{n}^1 is based on the tangent of the blue curve, \mathbf{n}^3 is the unit-vector pointing in x_3 -direction, and $\mathbf{n}^2 = \mathbf{n}^1 \times \mathbf{n}^3$.

For some types of microstructures it is easy to create an implicit geometry description based on a periodic function. A plate spanning the x_2x_3 -plane can be repeated in space using,

$$\psi(\mathbf{x}) = \frac{1}{2}(1 + S\{Px_1\}) - w(\mathbf{x}), \quad (7)$$

where $S \in [-1, 1]$ is a triangle wave and P is a periodicity scaling parameter. As can be seen in Figure 7(a) the microstructure width w can be spatially varying. Hence, we can easily create a sequence of spatially varying SSR3 microstructures in space. Similarly, we can use

mapping functions ϕ to create a sequence of spatially varying SSR3 microstructures using,

$$\psi_i(\mathbf{x}) = \frac{1}{2}(1 + S\{P_i\phi_i(\mathbf{x})\}) - w_i(\mathbf{x}), \quad i = 1, 2, 3. \quad (8)$$

An overview of a sequence of plates with spatially varying orientation can be seen in Figure 7(b). As discussed by Groen et al. (2020) and in Appendix B we can base periodicity scaling parameters P_i on an average unit-cell spacing ϵ . Furthermore, we can adjust layer widths w_i to make sure that a minimum feature size f_{min} is guaranteed. In Figure 7(c) this is demonstrated by using a uniform thickness everywhere compensating for the layer spatially varying layer spacing.

Finally, we can combine the three different implicit geometry descriptions ψ_i to a single microstructure description ψ_{SSR3} using a Boolean union operation,

$$\psi_{SSR3}(\mathbf{x}) = \max_{i=1,2,3} \{\psi_i(\mathbf{x})\}. \quad (9)$$

With the above-mentioned techniques it is possible to de-homogenize spatially varying microstructures such as the SSR3, PLS and TLS. For the SSR3 it is important that the vector fields describing the microstructure orientation \mathbf{n}^1 , \mathbf{n}^2 and \mathbf{n}^3 are smooth and continuous throughout the design domain. For the isotropic microstructures having a spatially varying orientation makes no sense; however, the plate or bar thickness can be spatially varying creating a graded design, where the coating can be included in the implicit geometry description using another Boolean union. As an example consider the coated structure using $6 \times 6 \times 12$ repetitions the uniform isotropic TLS shown in Figure 8. Furthermore, we can visually identify the difference between the coated and a non-coated design using Figure 9(b) and (c), for the cantilever s.t. a corner load using the SSR3 microstructure with a fixed orientation and $\epsilon = 1/10$.

4.2 Performance of a de-homogenized design using a constant microstructure

Besides comparing the elasticity tensor between a multi-scale and single-scale microstructure it is important to identify the difference in performance between a finite number of microstructures and the elasticity tensor approximated by numerical homogenization. Notable works in this aspect are the works by Hollister and Kikuchi (1992) and Pecullan et al. (1999) in 2D and by Coelho et al. (2016) in 3D. Besides the effect on the elasticity tensor, the works of Zhang and Sun (2006) and Zuo et al. (2013) identify the difference between a 2D multi-scale model with uniform microstructures and

a single-scale approximation for different amount of microstructure repetitions. Here we extend these studies to 3D using the cantilever subject to a downward corner load (Figure 5(a)). We use the isotropic TLS using a microstructure volume fraction $\rho = 0.25$. An example of the single-scale approximation using $6 \times 6 \times 12$ microstructures can be seen in Figure 8. Furthermore, the de-homogenized designs using $1 \times 1 \times 2$, $2 \times 2 \times 4$ and $3 \times 3 \times 6$ microstructure repetitions can be seen in Figure 10(a), (b), and (c) respectively.

Using nTop platform we can directly mesh the implicit geometry description using the meshing method proposed by Hu et al. (2018, 2019). For different numbers of microstructures n_{micro} we obtain meshes of around 1-3 million tetrahedral elements that are modeled using quadratic shape functions. To ensure that the analysis between the different structures is not influenced by the difference in the meshes we have included an analysis of the meshes using libigl (Jacobson et al., 2018). The number of finite elements $n_{elements}$, number of degrees of freedom n_{dof} , the mean edge length \bar{h} and the standard deviation σ_h are shown in Table 3. The compliance values for the two load-cases $\mathcal{J}^{f,1}$ and $\mathcal{J}^{f,2}$ correspond to a loading area of $L/10 \times L/10$ (load-case 1) and a loading area of $L/5 \times L/5$ (load-case 2) respectively. Furthermore, we show the performance using only the coating *i.e.* no microstructures, and the multi-scale performance on a fine mesh with a similar amount of degrees of freedom to avoid differences due to h -convergence (multi-scale fine). Finally, we have modeled the multi-scale design on a coarse regular mesh in MATLAB (multi-scale coarse) to show the modeling error between a coarse multi-scale mesh and a full-scale model on a fine mesh.

From Table 3, it can be seen that the difference in mean edge length is relatively constant between the different meshes. Combined with the large number of tetrahedral elements and order of the shape functions we believe that the mesh effects will not affect the comparison. The compliance values converge slowly towards the multi-scale performance with a relatively small difference (*i.e.* $< 5\%$), even for few microstructure repetitions. This indicates that for this example the single-scale approximation represents the multi-scale performance well. The fact that the difference between the multi-scale modeling and the single-scale interpretation is so small can be attributed to the efficient load-transfer between the infill and the solid coating that is used to avoid undesired boundary effects.

Furthermore, it is interesting to see that the compliance values converge from below towards the compliance of the multi-scale design. This is in line with numerical observations by Zhang and Sun (2006) and Zuo

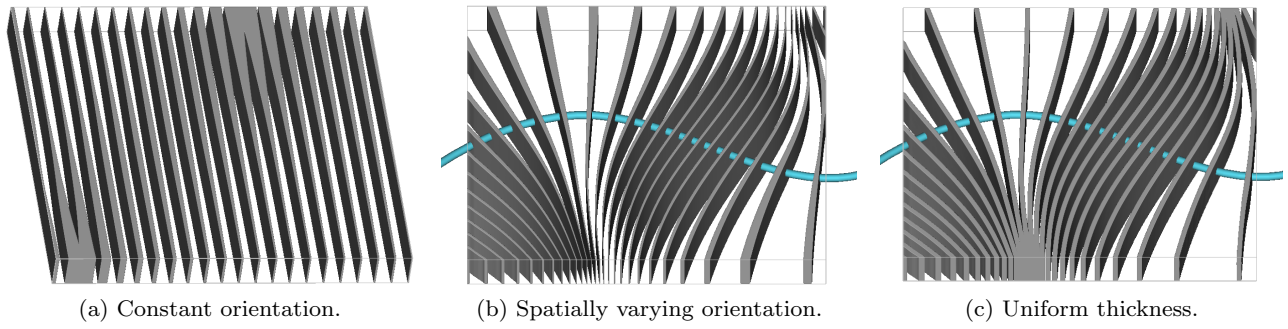
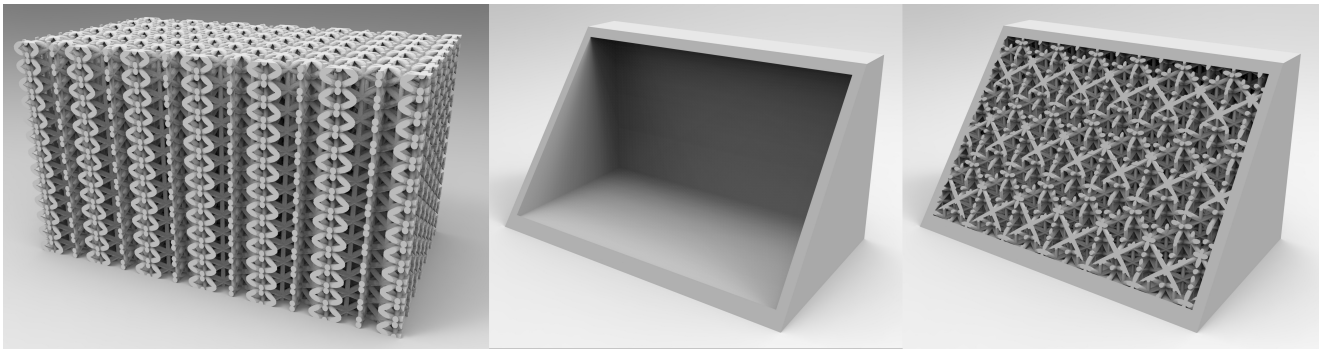
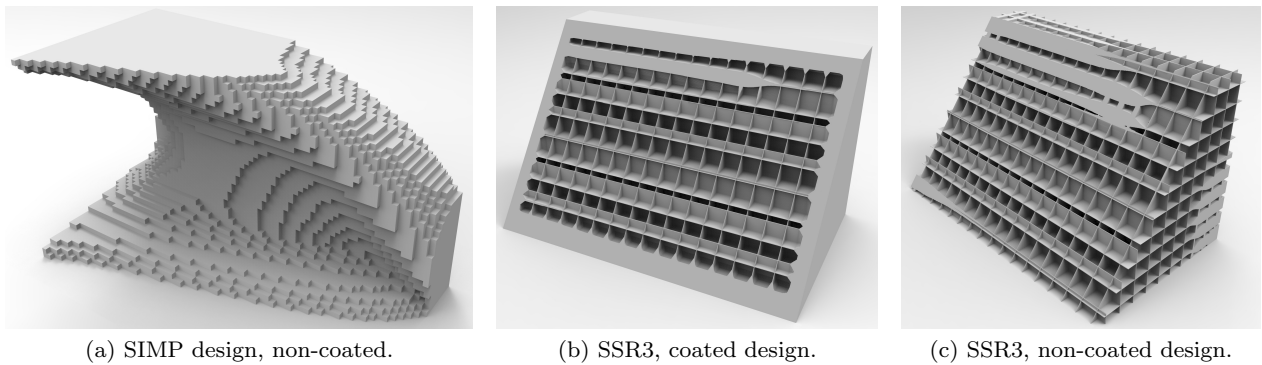


Fig. 7: Spatially varying sequence of plates.

Fig. 8: A single-scale approximation of multi-scale coated design using $6 \times 6 \times 12$ isotropic TLS microstructure repetitions shown left, the coating in the middle and the full design on the right.Fig. 9: SIMP design and cut sections of the de-homogenized designs for the cantilever s.t. a corner load. For the de-homogenized designs the SSR3 microstructure is used with a fixed orientation and $\epsilon = 1/10$.

et al. (2013). Furthermore, to make sure that the results are not biased by the microstructure location, we have shifted the infill for the designs 15% of the domain length in y -direction. For the infill with $1 \times 1 \times 2$ microstructure repetitions this resulted in $\mathcal{J}^{f,1} = 124.48$ and $\mathcal{J}^{f,2} = 106.13$, for a $2 \times 2 \times 4$ microstructure repetitions this resulted in $\mathcal{J}^{f,1} = 129.64$ and $\mathcal{J}^{f,2} = 105.03$ and for a $3 \times 3 \times 6$ microstructure repetitions this resulted in $\mathcal{J}^{f,1} = 125.59$ and $\mathcal{J}^{f,2} = 105.22$. As can be seen the difference in compliance is negligible which

can be attributed to the efficient load transfer between the infill and the coating. Hence, with this study we demonstrate that it is possible to mesh and analyze a single-scale approximation of a multi-scale design on a modern workstation PC. We invite other researchers to do the same to increase the reliability of multi-scale topology optimization methods and mature this field of research.

Finally, it has to be mentioned that the present studies are still quite limited in size and scope. Ideally

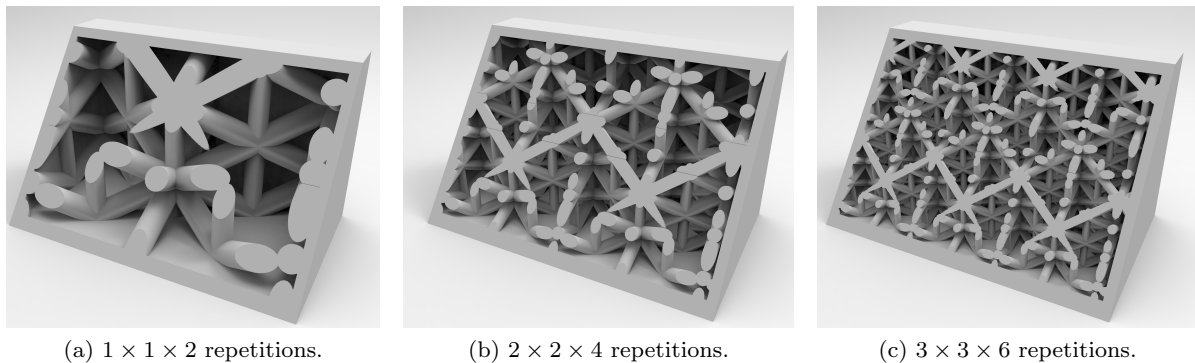


Fig. 10: Single-scale interpretations with varying numbers of microstructure repetitions of a coated multi-scale design using the uniform TLS microstructure.

Table 3: Single-scale interpretation of the cantilever s.t. a load in the bottom corner for different number of microstructures n_{micro} . The number of finite elements $n_{element}$, degrees of freedom n_{dof} , properties of the mesh and compliance values $\mathcal{J}^{f,1}$ and $\mathcal{J}^{f,2}$ are shown for load-case 1 and 2 respectively.

Repetitions	n_{micro}	$n_{element}(\times 10^6)$	$n_{dof}(\times 10^6)$	\bar{h}	σ_h	$\mathcal{J}^{f,1}$	$\mathcal{J}^{f,2}$
Only coating	0	2.73	10.6	0.0180	0.0028	166.74	146.07
$1 \times 1 \times 2$	2	0.98	4.39	0.0192	0.0040	122.69	102.45
$2 \times 2 \times 4$	16	1.45	6.94	0.0166	0.0046	125.32	104.65
$3 \times 3 \times 6$	54	2.43	11.8	0.0126	0.0054	123.77	104.81
$4 \times 4 \times 8$	128	3.82	18.8	0.0115	0.0042	126.45	105.03
$5 \times 5 \times 10$	250	2.37	12.3	0.0130	0.0051	126.21	105.28
$6 \times 6 \times 12$	432	2.79	15.0	0.0122	0.0052	128.21	105.55
multi-scale fine	∞	2.73	10.6	0.0180	0.0028	128.37	107.05
multi-scale coarse	∞	0.11	0.35	0.0250	0	126.24	105.61

we would like to model even more repetitions, different types of microstructures, loading cases and designs at a lower volume fraction.

4.3 Performance of a de-homogenized design using spatially varying microstructures

The Michell cantilever that is optimized using rank-3 microstructures and described in detail in Groen et al. (2020) and Table 2 is de-homogenized using nTop platform. The benefit of using this platform over de-homogenization on a voxel grid as done in Groen et al. (2020) is that we can capture the geometrical features much better without seeing jagged edges or using a very fine voxel mesh as can be seen in Figure 11. Since the implicit geometry can be converted directly into a tetrahedral mesh we do not need as many elements as for the voxel mesh. This means that the fine-scale validation of the de-homogenized designs can be performed on a modern workstation PC instead of on a high performance computing system with of 3200 cores as in (Groen et al., 2020).

The Michell cantilever optimized for a volume fraction $V_f^{max} = 0.10$ with dimensions $1 \times 2 \times 1$ is de-

homogenized with a minimum feature size of $f_{min} = 1/240$ and different values for average unit-cell spacing ϵ . These settings allow for a direct comparison with the results shown in Groen et al. (2020). However, before we can do a direct comparison it is important to make sure that the finite element analysis of the de-homogenized structure is accurate. To verify this we consider the case with $\epsilon = 6/120$, for which we have generated 5 different meshes, evaluated mesh properties using libigl (Jacobson et al., 2018) and subsequently performed finite element analysis. The number of tetrahedral elements n_{tet} , the mean edge length \bar{h} and the standard deviation σ_h and corresponding compliance values $\mathcal{J}^{f,1}$ and $\mathcal{J}^{f,2}$ for linear and quadratic shape functions respectively are shown in Table 4.

The compliance for linear finite elements $\mathcal{J}^{f,1}$ converges quadratically w.r.t \bar{h} , while $\mathcal{J}^{f,2}$ converges quadratically w.r.t \bar{h} (Cook et al., 2001). The corresponding convergence plot can be seen in Figure 12. From this figure we can conclude that the compliance value $\mathcal{J}^{f,2}$ for the finest mesh should give an accurate approximation of the "real" performance. Similarly, we assume that the design analyzed on a very fine voxel mesh using linear

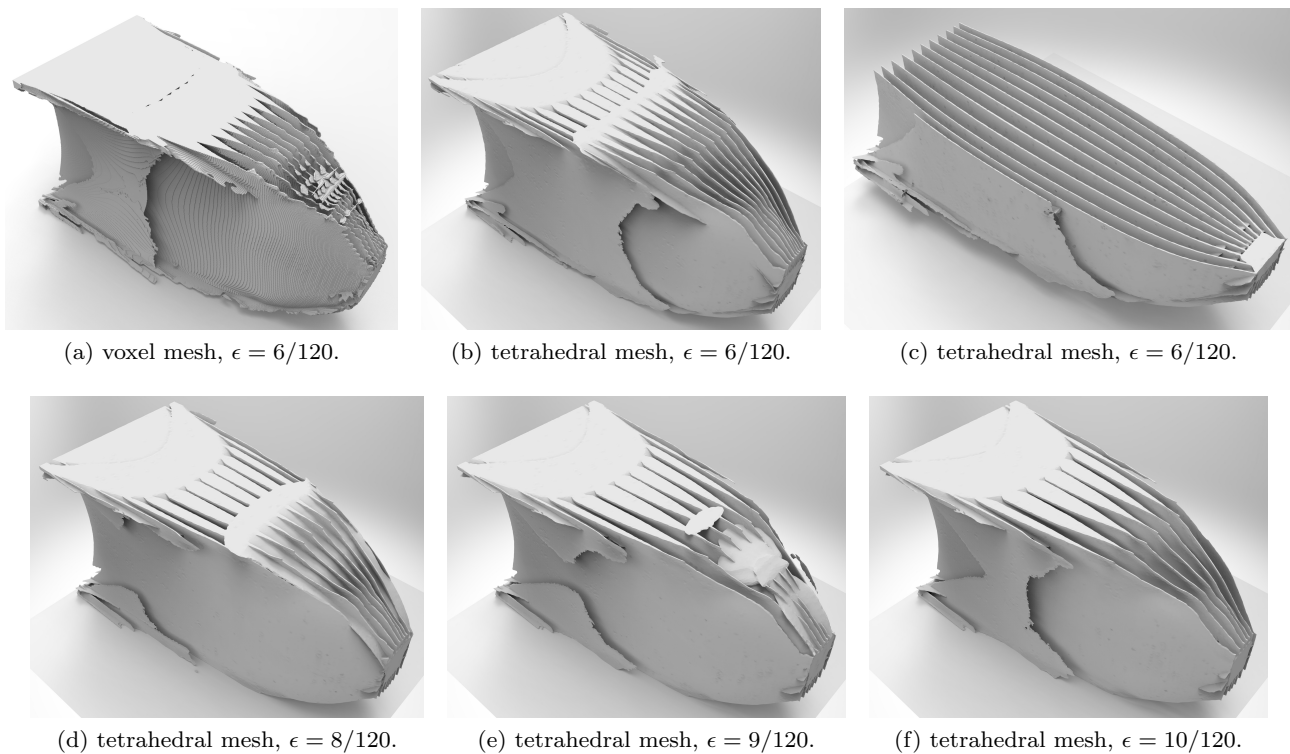


Fig. 11: The Michell cantilever de-homogenized for different values of ϵ with a minimum thickness of $f_{min} = 1/240$ using either a voxel mesh or a tetrahedral mesh.

Table 4: Compliance values $\mathcal{J}^{f,1}$ and $\mathcal{J}^{f,2}$ using linear and quadratic shape functions respectively for the de-homogenized Michell cantilever using $\epsilon = 6/120$. The effect of different number of tetrahedral elements n_{tet} and mean edge length \bar{h} and standard deviation in edge length σ_h is considered.

$n_{tet} (\times 10^5)$	\bar{h}	σ_h	$\mathcal{J}^{f,1}$	$\mathcal{J}^{f,2}$
1.23	0.03281	0.01796	213.07	221.67
3.90	0.02000	0.00657	218.79	225.66
6.29	0.01543	0.00638	220.16	226.36
6.70	0.01596	0.00442	220.34	226.44
16.3	0.01128	0.00256	222.34	227.13

shape function should be an accurate approximation of the "real" compliance as well.

The corresponding compliance values $\mathcal{J}^{f,2}$ for the finest quadratic tetrahedral meshes obtained for different values of ϵ can be seen in Table 5, while renders of the different meshes can be seen in Figure 11. The de-homogenization, mesh and analysis time T^f as well as the total run time T^{tot} are shown as well. Furthermore, the volume fraction of the de-homogenized design V_f^f and a measure for the stiffness per volume \mathcal{S} which is the compliance multiplied with the volume fraction are introduced. Finally, we repeat the results for the de-

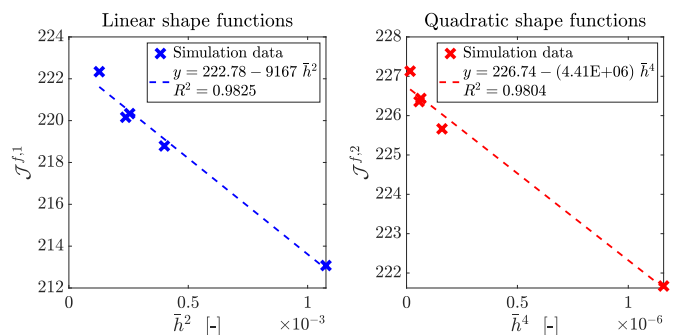


Fig. 12: Convergence plot of the compliance values $\mathcal{J}^{f,1}$ and $\mathcal{J}^{f,2}$ for linear and quadratic shape functions respectively for different meshes with different mean edge lengths \bar{h} .

homogenized designs on a voxel mesh from Groen et al. (2020) for comparison as well as the performance of a reference design obtained using the SIMP method and a continuation on the penalty parameter.

A first observation is that the de-homogenization, the meshing and the fine-scale analysis can all be done in less than 5 hours on a single PC. This is a big improvement compared to the method presented in Groen et al. (2020) where the post-analysis could only be done

Table 5: Compliance values \mathcal{J}^f , volume fractions V_f^f and measure for stiffness per volume \mathcal{S}^f of the de-homogenized designs for the Michell cantilever. The designs are de-homogenized for different values of average unit-cell spacing ϵ and on different meshes. Corresponding de-homogenization, mesh and analysis time T^f and total time T^{tot} including homogenization-based topology optimization are shown.

ϵ	Element type	$n_{element}(\times 10^6)$	\bar{h}	\mathcal{J}^f	V_f^f	\mathcal{S}^f	T^f	T^{tot}
5/120	Quadratic Tet	1.87	0.01107	222.33	0.1139	25.324	04:30:22	14:15:57
6/120	Quadratic Tet	1.63	0.01128	227.13	0.1087	24.685	04:08:55	13:54:30
7/120	Quadratic Tet	1.50	0.01141	232.22	0.1067	24.789	03:24:10	13:09:45
8/120	Quadratic Tet	1.42	0.01158	234.47	0.1067	25.014	02:54:57	12:40:32
9/120	Quadratic Tet	1.33	0.01164	254.91	0.1032	26.299	02:46:08	12:31:43
10/120	Quadratic Tet	1.25	0.01165	294.35	0.0987	28.946	03:31:49	13:17:24
6/120	Linear Hex	221	0.00208	235.96	0.1073	25.322	-	-
8/120	Linear Hex	221	0.00208	237.64	0.1061	25.219	-	-
10/120	Linear Hex	221	0.00208	237.14	0.1052	24.942	-	-
SIMP	Linear Hex	221	0.00208	236.26	0.1000	23.626	-	-

on a high performance computing system comprising 3200 cores. Hence, T^{tot} is not included for the voxel meshes. Nevertheless, we can compare the result to the cantilever obtained with SIMP method which took 08:13:28 on 3200 cores, which is roughly 26300 CPU hours. Compared to approximately 14 CPH hours on the workstation we can conclude that we have achieved a speed up factor of 1875! The combination of multi-scale topology optimization and de-homogenization and analysis using nTop platform thus brings us one step closer to making high-resolution topology optimization an interactive part of the design process.

Furthermore, it can be seen that the tetrahedral meshes are better at capturing the shape of the geometry than the voxel meshes. For lower values of ϵ the measure of stiffness per volume \mathcal{S}^f is slightly lower than for the voxel meshes. Nevertheless, we can still see a 5% deviation compared to the SIMP method, hence there is still room for improvement. Possible solutions can be to de-homogenize for even smaller values of ϵ , such that the de-homogenized design better represents the optimal multi-scale design it is based on. Although this can be done, the meshing on a normal workstation would be problematic due to the many small features involved. Therefore, we do not consider smaller values of ϵ in this work.

Finally, it can be seen that the compliance values for higher values of ϵ are far from optimal. The reason is that the peaks of the triangle waves are exactly at the boundary of the material domain of interest $\tilde{\Omega}_i$, which means that the vertical webs are sometimes cut-off. This can be seen in Figure 11(d)-(f) where the non-load carrying part progressively takes up a bigger part of the structure, and the effect is also discussed for the 2D case in (Groen and Sigmund, 2018). A possible solution would be to make sure that the minimum values of the triangle waves intersect with the boundary of $\tilde{\Omega}_i$;

however, such an approach will be pursued in a future work.

5 Concluding remarks

We have given a discussion on the state-of-the-art of multi-scale topology optimization to get high-resolution designs in a relatively short time. To do this, we have shown that when stiffness is considered, graded isotropic plate lattice structures (PLS) outperform their open-walled counter parts, the isotropic truss lattice structures (TLS). As expected even better performing designs can be obtained when using near-optimal graded anisotropic microstructures. However, we have shown that restricting either the density, widths or orientation of the microstructures has a large influence on the performance allowing the SIMP method to provide better results. Hence, when doing multi-scale optimization the microstructure parameterization has to be carefully selected. A limitation of this study is that only compliance minimization for a single loading case is considered. In a future study multiple load-cases should be considered for which a single-scale approximation of a rank-6 microstructure can be used. Furthermore, it is important that other problems than compliance are considered. Possibly, optimization of a fundamental frequency or stress constrained topology optimization.

Furthermore, we have shown how implicit geometry descriptions can be used to get single-scale approximations of multi-scale designs. Using nTop platform (nTopology Inc, 2020) we can generate high-resolution geometries that can be meshed and subsequently analyzed. We have demonstrated the small difference in performance between multi-scale performance and a full-scale analysis validating the proposed de-homogenization method. We have been able to de-homogenize an optimal multi-scale design and do the full-scale validation

on a modern workstation PC. This means that compared to density-based topology optimization we can now do ultra large-scale topology optimization on a single PC resulting in a reduction in computational cost of at least 3 orders of magnitude. Hence the presented method is an improvement compared to (Groen et al., 2020) where a HPC system consisting of 3200 cores was used for the full-scale validation.

Finally, we have demonstrated the importance of verifying the performance of the single-scale interpretations of multi-scale designs. We hope that we hereby can inspire others working in the field to perform similar verification studies.

Acknowledgements The authors acknowledge the support of the Villum Fonden through the Villum investigator project InnoTop and the support of nTopology inc. The first author is indebted to Yiqiang Wang and the simulation team at nTopology inc. for valuable discussions during the preparation of this manuscript. Finally, the authors would like to thank Krister Svanberg for providing the MATLAB MMA code.

Conflict of interest

The authors declare that they have no conflict of interest.

Replication of results

Our work relies on several methodologies implemented in either MATLAB or nTop platform. Specifically, the homogenization-based topology optimization has been performed in MATLAB, the methodology to do so has been discussed in detail in (Groen, 2019; Groen et al., 2020) and the reader is referred to these works for more details. The numerical homogenization, de-homogenization, meshing and fine-scale analysis have been performed using nTop platform (nTopology Inc, 2020), details about this software platform can be found on <https://support.ntopology.com/hc/en-us>.

Appendix A: Universal isotropy index

The universal isotropy index M^U is obtained as (Ranganathan and Ostoja-Starzewski, 2008),

$$M^U = 5 \frac{G^V}{G^R} + \frac{K^V}{K^R} - 6, \quad (10)$$

here the superscripts V and R indicate the Voigt and Reuss measurements of the shear modulus G and bulk modulus K .

These measurements can be obtained as (Hill, 1952),

$$\begin{aligned} K^V &= \frac{\tilde{E}_{1111}}{3} + \frac{2\tilde{E}_{1122}}{3}, \\ G^V &= \frac{\tilde{E}_{1111}}{5} - \frac{\tilde{E}_{1122}}{5} + \frac{3\tilde{E}_{1212}}{5}, \\ K^R &= \left(3\tilde{S}_{1111} + 6\tilde{S}_{1122}\right)^{-1}, \\ G^R &= \left(\frac{4\tilde{S}_{1111}}{5} - \frac{4\tilde{S}_{1122}}{5} + \frac{12\tilde{S}_{1212}}{5}\right)^{-1}, \end{aligned} \quad (11)$$

with compliance tensor $\mathbf{S} = \mathbf{E}^{-1}$ and,

$$\begin{aligned} \tilde{E}_{1212} &= \frac{E_{1212} + E_{1313} + E_{2323}}{3}, \\ \tilde{S}_{1111} &= \frac{S_{1111} + S_{2222} + S_{3333}}{3}, \\ \tilde{S}_{1122} &= \frac{S_{1122} + S_{1133} + S_{2233}}{3}, \\ \tilde{S}_{1212} &= \frac{S_{1212} + S_{1313} + S_{2323}}{3}. \end{aligned} \quad (12)$$

Appendix B: Mapping functions ϕ from spatially varying orientation

In this Section we summarize the methodology presented in Groen et al. (2020) to obtain smooth and continuous mapping functions $\phi = \{\phi_1, \phi_2, \phi_3\}$ from 3 smooth and continuous orthogonal vector fields $\{\mathbf{n}^1, \mathbf{n}^2, \mathbf{n}^3\}$. The theory to extract these smooth and continuous vector fields from the optimized microstructure orientation is discussed in more detail in Groen et al. (2020).

From Equations 8 and 9 it follows that if a lamination direction has no width *i.e.* $w_i = 0$ it is not important how the corresponding mapping function ϕ_i looks. Furthermore, if a microstructure is solid *i.e.* $\rho = 1$, than all mapping functions at that point can be relaxed. Hence, we require only an accurate description of ϕ_i in Ω_i ,

$$\mathbf{x} \in \Omega_i \quad \text{if} \quad w_i(\mathbf{x}) > 0.01 \quad \text{and} \quad \rho(\mathbf{x}) < 0.99. \quad (13)$$

To solve for ϕ_i we solve the following least-squares problem,

$$\begin{aligned} \min_{\phi_i(\mathbf{x})} : \mathcal{I}(\phi_i(\mathbf{x})) &= \frac{1}{2} \int_{\Omega} \alpha_1^i(\mathbf{x}) \|\nabla \phi_i(\mathbf{x}) - \mathbf{n}^i(\mathbf{x})\|^2 d\Omega, \\ \text{s.t.} : \alpha_2^i(\mathbf{x}) \nabla \phi_i(\mathbf{x}) \cdot \mathbf{t}^{i,1}(\mathbf{x}) &= 0, \\ \text{s.t.} : \alpha_2^i(\mathbf{x}) \nabla \phi_i(\mathbf{x}) \cdot \mathbf{t}^{i,2}(\mathbf{x}) &= 0. \end{aligned} \quad (14)$$

Here $\mathbf{t}^{i,1}$ and $\mathbf{t}^{i,2}$ span a plane tangent to \mathbf{n}^i *i.e.* for \mathbf{n}^1 we have $\mathbf{t}^{1,1} = \mathbf{n}^2$ and $\mathbf{t}^{1,2} = \mathbf{n}^3$. The domain is split into three parts, which dictate the weights on the objective α_1^i and the weights on the constraints α_2^i that allow us to relax ϕ_i outside Ω_i ,

$$\begin{aligned} \alpha_1^i(\mathbf{x}) &= \begin{cases} 0.01 & \text{if } w_i(\mathbf{x}) < 0.01, \\ 0.10 & \text{if } \rho(\mathbf{x}) > 0.99, \\ 1.00 & \text{if } \mathbf{x} \in \Omega_i, \end{cases} \\ \alpha_2^i(\mathbf{x}) &= \begin{cases} 0.00 & \text{if } w_i(\mathbf{x}) < 0.01, \\ 0.00 & \text{if } \rho(\mathbf{x}) > 0.99, \\ 1.00 & \text{if } \mathbf{x} \in \Omega_i. \end{cases} \end{aligned} \quad (15)$$

Numerically, the above-mentioned problem can be solved using a finite element approach on a regular grid. Where the grid can be of similar resolution as \mathcal{T}^c . Furthermore, the constraints are enforced in an augmented setting using a penalty parameter $\gamma_\phi = 1000$. We can impose an average unit-cell spacing ϵ . To do so, we define the periodicity scaling parameter P_i based on the average lattice spacing in the domain of interest $\tilde{\Omega}_i$,

$$P_i = \frac{2\pi}{\epsilon} \frac{\int_{\tilde{\Omega}_i} d\tilde{\Omega}_i}{\int_{\tilde{\Omega}_i} \|\nabla\phi_i(\mathbf{x})\| d\tilde{\Omega}_i}. \quad (16)$$

From the mapping function ϕ_i we can identify the local distance between each plate λ_i using,

$$\lambda_i(\mathbf{x}) = \frac{2\pi}{P_i \|\nabla\phi_i(\mathbf{x})\|}. \quad (17)$$

This local spacing can be used to get a description of the actual feature size of the geometry f_i for each lamination direction i .

$$f_i(\mathbf{x}) = w_i(\mathbf{x})\lambda_i(\mathbf{x}). \quad (18)$$

This description can then be used to modify the width w_i to add a minimum feature size f_{min} to avoid very thin plates. Another option can be to impose a uniform feature size f_i in the entire domain, as can be seen in Figure 7(c).

References

- Aage, N., Andreassen, E., Lazarov, B.S., Sigmund, O., 2017. Giga-voxel computational morphogenesis for structural design. *Nature* 550, 84–86. doi:10.1038/nature23911.
- Alexandersen, J., Lazarov, B., 2015. Topology optimisation of manufacturable microstructural details without length scale separation using a spectral coarse basis preconditioner. *Computer Methods in Applied Mechanics and Engineering* 290, 156–182. doi:10.1016/j.cma.2015.02.028.
- Allaire, G., 2002. *Shape Optimization by the Homogenization Method*. Springer-Verlag, New York.
- Allaire, G., Aubry, S., 1999. On optimal microstructures for a plane shape optimization problem. *Structural optimization* 17, 86–94. doi:10.1007/BF01195933.
- Amir, O., Aage, N., Lazarov, B.S., 2013. On multigrid-cg for efficient topology optimization. *Structural and Multidisciplinary Optimization* 49, 815–829. doi:10.1007/s00158-013-1015-5.
- Andersen, M.N., Wang, F., Sigmund, O., 2020. On the competition for ultimately stiff and strong architected materials. *Proceedings of the National Academy of Sciences of the United States of America* (submitted), 1–28.
- Ansys Inc, 2020. Ansys mechanical. URL: <https://www.ansys.com/products/structures>.
- Autodesk Inc, 2020. Autodesk fusion 360®. URL: <https://www.autodesk.com/products/fusion-360/overview>.
- Bendsøe, M., Kikuchi, N., 1988. Generating optimal topologies in structural design using a homogenization method. *Computer Methods in Applied Mechanics and Engineering* 71, 197–224. doi:10.1016/0045-7825(88)90086-2.
- Bendsøe, M., Sigmund, O., 2004. *Topology optimization-theory, methods, and applications*. Springer, Berlin.
- Bensoussan, A., Lions, J.L., Papanicolaou, G., 1978. *Asymptotic Analysis for Periodic Structures (Studies in mathematics and its applications)*. Elsevier Science Ltd.
- Bourdin, B., 2001. Filters in topology optimization. *International Journal for Numerical Methods in Engineering* 50, 2143–2158. doi:10.1002/nme.116.
- Brackett, D., Ashcroft, I., Hague, R., 2011. Topology optimization for additive manufacturing. *22nd Annual International Solid Freeform Fabrication Symposium - An Additive Manufacturing Conference, SFF 2011*, 348–362.
- Bruns, T., Tortorelli, D., 2001. Topology optimization of nonlinear elastic structures and compliant mechanisms. *Computer Methods in Applied Mechanics and Engineering* 190, 3443–3459. doi:10.1016/S0045-7825(00)00278-4.
- Christensen, R., 1986. Mechanics of low density materials. *Journal of the Mechanics and Physics of Solids* 34, 563–578. doi:10.1016/0022-5096(86)90037-2.
- Clausen, A., Aage, N., Sigmund, O., 2015. Topology optimization of coated structures and material interface problems. *Computer Methods in Applied Mechanics and Engineering* 290, 524–541. doi:10.1016/j.cma.2015.02.011.
- Clausen, A., Aage, N., Sigmund, O., 2016. Exploiting additive manufacturing infill in topology optimization for improved buckling load. *Engineering* 2, 250–257. doi:10.1016/J.ENG.2016.02.006.
- Coelho, P., Amiano, L., Guedes, J., Rodrigues, H., 2016. Scale-size effects analysis of optimal periodic material microstructures designed by the inverse homogenization method. *Computers & Structures* 174, 21–32. doi:10.1016/j.compstruc.2015.10.001.
- COMSOL Inc, 2019. Comsol multiphysics®5.5. URL: <https://www.comsol.com>.
- Cook, R.D., Malkus, D.S., Plesha, M.E., 2001. *Concepts and Applications of Finite Element Analysis*. Wiley.
- Cramer, A.D., Challis, V.J., Roberts, A.P., 2015. Microstructure interpolation for macroscopic design. *Structural and Multidisciplinary Optimization* 53, 489–500. doi:10.1007/s00158-015-1344-7.
- Dassault Systèmes, 2020. 3dexperience release r2021x. URL: <https://www.3ds.com/products-services/simulia/products/3dexperience>.
- Du, Z., Zhou, X., Picelli, R., Kim, H., 2018. Connecting microstructures for multiscale topology optimization with connectivity index constraints. *ASME: Journal of Mechanical Design* 140, 1–12. doi:10.1115/1.4041176.
- Francfort, G.A., Murat, F., 1986. Homogenization and optimal bounds in linear elasticity. *Archive for Rational Mechanics and Analysis* 94, 307–334. doi:10.1007/BF00280908.
- Fu, J., Li, H., Gao, L., Xiao, M., 2019. Design of shell-infill structures by a multiscale level set topology optimization method. *Computers & Structures* 212, 162–172. doi:10.1016/j.compstruc.2018.10.006.
- Garner, E., Kolken, H.M., Wang, C.C., Zadpoor, A.A., Wu, J., 2019. Compatibility in microstructural optimization for additive manufacturing. *Additive Manufacturing* 26, 65–75. doi:10.1016/j.addma.2018.12.007.
- Geoffroy-Donders, P., 2018. Homogenization method for topology optimization of structures built with lattice materials. *Theses. Ecole Polytechnique*.
- Geoffroy-Donders, P., Allaire, G., Michailidis, G., Pantz, O., 2020a. Coupled optimization of macroscopic structures and lattice infill. *International Journal for Numerical Methods in Engineering* doi:10.1002/nme.6392.
- Geoffroy-Donders, P., Allaire, G., Pantz, O., 2020b. 3-d topology optimization of modulated and oriented periodic microstructures by the homogenization method. *Journal of Computational Physics* 401, 108994. doi:10.1016/j.jcp.2019.108994.

- Gibiansky, L.V., Cherkaev, A.V., 1987. Microstructures of composites of extremal rigidity and exact estimates of the associated energy density. Report 1115. Ioffe Physico-Technical Institute, Acad of Sc, USSR. Leningrad, USSR. English translation in: Cherkaev, A.V., Kohn, R.V. (Eds), 1997. Topics in the mathematical modelling of composite materials. Birkhäuser Boston, MA.
- Groen, J.P., 2019. Multi-Scale Design Methods for Topology Optimization. Ph.D. thesis.
- Groen, J.P., Sigmund, O., 2018. Homogenization-based topology optimization for high-resolution manufacturable microstructures. *International Journal for Numerical Methods in Engineering* 113, 1148–1163. doi:10.1002/nme.5575.
- Groen, J.P., Stutz, F.C., Aage, N., Bærentzen, J.A., Sigmund, O., 2020. De-homogenization of optimal multi-scale 3d topologies. *Computer Methods in Applied Mechanics and Engineering* 364, 112979. doi:10.1016/j.cma.2020.112979.
- Groen, J.P., Wu, J., Sigmund, O., 2019. Homogenization-based stiffness optimization and projection of 2d coated structures with orthotropic infill. *Computer Methods in Applied Mechanics and Engineering* 349, 722 – 742. doi:10.1016/j.cma.2019.02.031.
- Hashin, Z., Shtrikman, S., 1963. A variational approach to the theory of the elastic behaviour of multiphase materials. *Journal of the Mechanics and Physics of Solids* 11, 127–140. doi:10.1016/0022-5096(63)90060-7.
- Hill, R., 1952. The elastic behaviour of a crystalline aggregate. *Proceedings of the Physical Society. Section A* 65, 349.
- Hollister, S.J., Kikuchi, N., 1992. A comparison of homogenization and standard mechanics analyses for periodic porous composites. *Computational Mechanics* 10, 73–95. doi:10.1007/bf00369853.
- Hu, Y., Schneider, T., Wang, B., Zorin, D., Panozzo, D., 2019. Fast tetrahedral meshing in the wild. [arXiv:1908.03581](https://arxiv.org/abs/1908.03581).
- Hu, Y., Zhou, Q., Gao, X., Jacobson, A., Zorin, D., Panozzo, D., 2018. Tetrahedral meshing in the wild. *ACM Transactions on Graphics* 37, 1–14. doi:10.1145/3197517.3201353.
- Huang, X., Zhou, S., Xie, Y., Li, Q., 2013. Topology optimization of microstructures of cellular materials and composites for macrostructures. *Computational Materials Science* 67, 397–407. doi:10.1016/j.commatsci.2012.09.018.
- Jacobson, A., Panozzo, D., et al., 2018. libigl: A simple C++ geometry processing library. URL: <https://libigl.github.io/>.
- Jiang, L., Gu, X.D., Chen, S., 2020. Generative design of bionic structures via concurrent multiscale topology optimization and conformal geometry method. *Journal of Mechanical Design* 143. doi:10.1115/1.4047345.
- Jiang, L., Guo, Y., Chen, S., Wei, P., Lei, N., Gu, X.D., 2019. Concurrent optimization of structural topology and infill properties with a CBF-based level set method. *Frontiers of Mechanical Engineering* 14, 171–189. doi:10.1007/s11465-019-0530-5.
- Kohn, R.V., Strang, G., 1986. Optimal design and relaxation of variational problems, i. *Communications on Pure and Applied Mathematics* 39, 113–137. doi:10.1002/cpa.3160390107.
- Kumar, T., Suresh, K., 2019. A density-and-strain-based k-clustering approach to microstructural topology optimization. *Structural and Multidisciplinary Optimization* 61, 1399–1415. doi:10.1007/s00158-019-02422-4.
- Liu, C., Du, Z., Zhang, W., Zhu, Y., Guo, X., 2017. Additive manufacturing-oriented design of graded lattice structures through explicit topology optimization. *Journal of Applied Mechanics* 84. doi:10.1115/1.4036941.
- Liu, J., Gaynor, A.T., Chen, S., Kang, Z., Suresh, K., Takezawa, A., Li, L., Kato, J., Tang, J., Wang, C.C.L., Cheng, L., Liang, X., To, A.C., 2018. Current and future trends in topology optimization for additive manufacturing. *Structural and Multidisciplinary Optimization* 57, 2457–2483. doi:10.1007/s00158-018-1994-3.
- Liu, L., Yan, J., Cheng, G., 2008. Optimum structure with homogeneous optimum truss-like material. *Computers & Structures* 86, 1417 – 1425. doi:10.1016/j.compstruc.2007.04.030. structural Optimization.
- Luo, Y., Li, Q., Liu, S., 2019. A projection-based method for topology optimization of structures with graded surfaces. *International Journal for Numerical Methods in Engineering* 118, 654–677. doi:10.1002/nme.6031.
- Lurie, K.A., Cherkaev, A.V., 1984. G-closure of a set of anisotropically conducting media in the two-dimensional case. *Journal of Optimization Theory and Applications* 42, 283–304. doi:10.1007/BF00934300.
- Milton, G.W., 1986. Modelling the properties of composites by laminates, in: Ericksen, J.L., Kinderlehrer, D., Kohn, R., Lions, J.L. (Eds.), *Homogenization and Effective Moduli of Materials and Media*, Springer New York, New York, NY. pp. 150–174.
- Norris, A., 1985. A differential scheme for the effective moduli of composites. *Mechanics of Materials* 4, 1–16. doi:10.1016/0167-6636(85)90002-x.
- nTopology Inc, 2020. ntop platform@2.xx. URL: <https://ntopology.com>.
- Pantz, O., Trabelsi, K., 2008. A post-treatment of the homogenization method for shape optimization. *SIAM Journal on Control and Optimization* 47, 1380–1398. doi:10.1137/070688900.
- Pecullan, S., Gibiansky, L., Torquato, S., 1999. Scale effects on the elastic behavior of periodic and hierarchical two-dimensional composites. *Journal of the Mechanics and Physics of Solids* 47, 1509–1542. doi:10.1016/s0022-5096(98)00111-2.
- Ranganathan, S.I., Ostojja-Starzewski, M., 2008. Universal elastic anisotropy index. *Physical Review Letters* 101. doi:10.1103/physrevlett.101.055504.
- Rodrigues, H., Guedes, J., Bendsøe, M., 2002. Hierarchical optimization of material and structure. *Structural and Multidisciplinary Optimization* 24, 1–10. doi:10.1007/s00158-002-0209-z.
- Sigmund, O., 1994. Materials with prescribed constitutive parameters: An inverse homogenization problem. *International Journal of Solids and Structures* 31, 2313–2329. doi:10.1016/0020-7683(94)90154-6.
- Sivapuram, R., Dunning, P.D., Kim, H.A., 2016. Simultaneous material and structural optimization by multiscale topology optimization. *Structural and Multidisciplinary Optimization* 54, 1267–1281. doi:10.1007/s00158-016-1519-x.
- Svanberg, K., 1987. The method of moving asymptotes—a new method for structural optimization. *International Journal for Numerical Methods in Engineering* 24, 359–373. doi:10.1002/nme.1620240207.
- Träff, E., Sigmund, O., Groen, J.P., 2019. Simple single-scale microstructures based on optimal rank-3 laminates. *Structural and Multidisciplinary Optimization* 59, 1021–1031. doi:10.1007/s00158-018-2180-3.
- Vermaak, N., Michailidis, G., Parry, G., Estevez, R., Allaire, G., Bréchet, Y., 2014. Material interface effects on the topology optimization of multi-phase structures using a level set method. *Structural and Multidisciplinary Opti-*

- mization 50, 623–644. doi:10.1007/s00158-014-1074-2.
- Wang, Y., Chen, F., Wang, M.Y., 2017. Concurrent design with connectable graded microstructures. *Computer Methods in Applied Mechanics and Engineering* 317, 84–101. doi:10.1016/j.cma.2016.12.007.
- Wang, Y., Groen, J.P., Sigmund, O., 2019. Simple optimal lattice structures for arbitrary loadings. *Extreme Mechanics Letters* 29, 100447. doi:10.1016/j.eml.2019.03.004.
- Wang, Y., Kang, Z., 2018. A level set method for shape and topology optimization of coated structures. *Computer Methods in Applied Mechanics and Engineering* 329, 553–574. doi:10.1016/j.cma.2017.09.017.
- Wang, Y., Sigmund, O., 2019. Quasiperiodic mechanical metamaterials with extreme isotropic stiffness. *Extreme Mechanics Letters* , 100596doi:10.1016/j.eml.2019.100596.
- Wu, J., Clausen, A., Sigmund, O., 2017. Minimum compliance topology optimization of shell-infill composites for additive manufacturing. *Computer Methods in Applied Mechanics and Engineering* 326, 358–375. doi:10.1016/j.cma.2017.08.018.
- Wu, J., Wang, W., Gao, X., 2019. Design and optimization of conforming lattice structures. *IEEE Transactions on Visualization and Computer Graphics* , 1–1doi:10.1109/TVCG.2019.2938946.
- Xue, D., Zhu, Y., Guo, X., 2020. Generation of smoothly-varying infill configurations from a continuous menu of cell patterns and the asymptotic analysis of its mechanical behaviour. *Computer Methods in Applied Mechanics and Engineering* 366, 113037. doi:10.1016/j.cma.2020.113037.
- Zhang, W., Sun, S., 2006. Scale-related topology optimization of cellular materials and structures. *International Journal for Numerical Methods in Engineering* 68, 993–1011. doi:10.1002/nme.1743.
- Zhou, S., Li, Q., 2008. Design of graded two-phase microstructures for tailored elasticity gradients. *Journal of Materials Science* 43, 5157–5167. doi:10.1007/s10853-008-2722-y.
- Zuo, Z.H., Huang, X., Yang, X., Rong, J.H., Xie, Y.M., 2013. Comparing optimal material microstructures with optimal periodic structures. *Computational Materials Science* 69, 137–147. doi:10.1016/j.commatsci.2012.12.006.